Atomistic Conversion Reaction Mechanism of WO_3 in Secondary Ion Batteries of Li, Na, and Ca

Yang He[+], Meng Gu[+], Haiyan Xiao, Langli Luo, Yuyan Shao, Fei Gao,* Yingge Du,*
Scott X. Mao,* and Chongmin Wang*

Abstract: _Intercalation and conversion are two fundamental chemical processes for battery materials in response to ion insertion. The interplay between these two chemical processes has never been directly seen and understood at atomic scale. Here, using in situ HRTEM, we captured the atomistic conversion reaction processes during Li, Na, Ca insertion into a WO_3 single crystal model electrode. An intercalation step prior to conversion is explicitly revealed at atomic scale for the first time for Li, Na, Ca. Nanoscale diffraction and ab initio molecular dynamic simulations revealed that after intercalation, the inserted ion–oxygen bond formation destabilizes the transition-metal framework which gradually shrinks, distorts and finally collapses to an amorphous W and M_xO (M = Li, Na, Ca) composite structure. This study provides a full atomistic picture of the transition from intercalation to conversion, which is of essential importance for both secondary ion batteries and electrochromic devices._

Conversion-type lithium ion batteries (LIB) using electrodes such as transition metal oxides, hydrides, and sulfides are capable of utilizing all possible oxidation states of a compound, and thus can provide large specific capacity for advanced applications such as electrical vehicles.[1] Under-

standing the atomistic conversion mechanism is fundamentally important in searching for new conversion-type electrode materials and the application of these materials.[2] Unfortunately, the conversion mechanism has not been explicitly established mostly because the process is wrapped in a nanoscale narrow reaction front. By atomistic simulations and detecting traces of intermediate phase, it is proposed that the conversion process is likely initiated by ion intercalation into the electrode materials, such as FeF_2,[2d] SnO_2,[3] Co_3O_4,[4] Fe_2O_3,[5] RuO_2,[6] MoO_3[7] and WO_3.[8] However, the methods including X-ray diffraction and selected area electron diffraction from a broad area across the reaction front are too ensemble-averaged to clearly resolve the relation between the intercalation and conversion. Besides, how the crystalline intercalation phase evolves to fully-charged conversion phases lacks detailed experimental investigation at the atomic scale. Here, using nano-beam diffraction (NBD) and electron energy loss spectroscopy (EELS) coupled with scanning/transmission electron microscopy (S/TEM), we investigated the structural and chemical evolution across a conversion reaction front with high spatial resolution in WO_3 upon insertion of electrochemical ions (Li, Na, Ca).

WO_3 is an ideal model system to study the intercalation-initiated conversion reaction, and the interplay between these two chemical processes. It is a widely studied electrochromic material as its pseudo-cubic cell contains a large, empty center site, providing an open environment for reversible intercalation/removal of small ions (e.g., H and Li). Due to the same reason and the high valence state that can theoretically host a maximum of 6 alkali metal ions or 3 alkaline earth metal ions,[7,9] WO_3 has also received interest as a candidate of conversion-type anode for next generation multivalent ion batteries.[10]

The test setup is shown in Figure 1a. Single-crystalline WO_3 films grown epitaxially on conductive Nb-doped $SrTiO_3$-(001) (Nb-STO) substrates by molecular beam epitaxy was used as electrodes in a half solid-cell setup. Details on film growth and characterization have been published elsewhere.[11] Electron diffraction (inset in Figure 1c) indicates that as-grown WO_3 has a monoclinic structure (space group $P21/c$), which is in good agreement with WO_3 used in LIB.[9b] The hetero-epitaxial architecture provides high mechanical stability for high-resolution TEM imaging and guarantees good electrical contact through conductive Nb-STO. Pure metals of Li, Na, and Ca were used as ion sources. The surface oxides due to short-time air-exposure, that is, Li_2O, Na_2O, and CaO, worked as electrolytes for ions. The ion source is manipulated by piezo-system to contact the WO_3 electrode at

[*] M. Gu,[+] L. Luo, Y. Du, C. Wang
Environmental Molecular Sciences Laboratory
Pacific Northwest National Laboratory
Richland, WA 99352 (USA)
E-mail: yingge.du@pnnl.gov
chongmin.wang@pnnl.gov

Y. He,[+] S. X. Mao
Department of Mechanical Engineering and Materials Science
University of Pittsburgh
Pittsburgh, PA 15261 (USA)
E-mail: sxm2@pitt.edu

H. Xiao
School of Physical Electronics
University of Electronic Science and Technology of China
Chengdu, 610054 (China)

Y. Shao
Energy and Environmental Directorate
Pacific Northwest National Laboratory
Richland, WA 99352 (USA)

F. Gao
Department of Nuclear Engineering and Radiological Sciences
University of Michigan
Ann Arbor, MI 48109 (USA)
E-mail: gaofeium@umich.edu

[+] These authors contributed equally to this work.

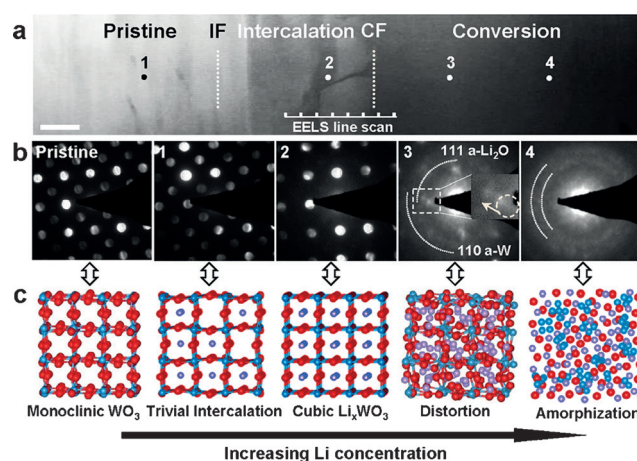Supporting information for this article can be found under:
http://dx.doi.org/10.1002/anie.201601542.
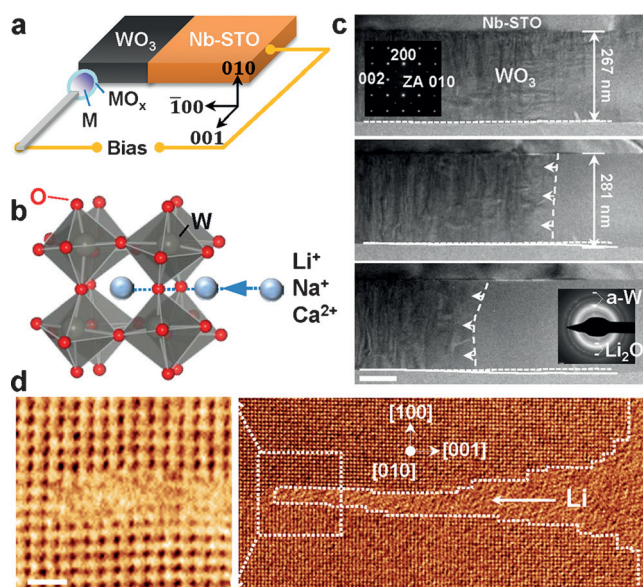
Figure 1. a) Setup of the in situ experiment (M = Li, Na, Ca). b) Atomic structural model of monoclinic WO_3 showing WO_6 octahedral and vacant site with Li (Na, or Ca) transporting along the channel into the vacant center site. c) Sequential TEM bright-field images showing WO_3 structure evolution during Li insertion (lithiation). Insets show electron diffraction patterns of pristine and fully lithiated phases. White dashed lines mark the reaction front or the surface position highlighting the volume expansion. Scale bar, 100 nm. d) High-resolution TEM image of a local region on the reaction front (dashed line). Inset on left is an atomic resolution annular dark field image of the boxed region. Scale bar, 1 nm.

Figure 2. a) High angle annular dark field (HAADF) scanning transmission electron microscopy (STEM) image of the reaction front in Figure 1c. Scale bar, 50 nm. b) Nano beam diffractions (NBD) from the pristine sample and across the conversion front (CF). c) Structure and crystal symmetry evolution with increasing Li concentration in the Li_xWO_3 lattice as indicated by the corresponding NBDs.

one end, and then biased (−0.8 V) with respect to the WO_3 film to drive the electrochemical reaction.

General morphology evolution of WO_3 during Li^+ insertion is shown by the sequential bright-field TEM images in Figure 1c. The reaction front (white dashed line in Figure 1c) is roughly perpendicular to WO_3 [001] direction, implying that Li atoms diffused along [010] lattice channel. This claim is supported by the atomic resolution images in Figure 1d which shows a reaction front penetrating along ⟨001⟩ into the lattice. Different from many other electrode materials,[3b,12] there was no high density dislocations, or "Medusa" zone, at the propagating reaction front (Supporting Movie 1), which can be attributed to the small volume expansion as a result of the spacious lattice channels (3.8 Å) for ion conduction in WO_3. Assuming equal expansion along three ⟨001⟩ directions, the volume expansion at full lithiation was estimated to be 17%, which was much lower than SnO_2[12] or Si (300%).[13] After fully charged with Li, the crystalline WO_3 was converted to amorphous W (a-W) metal and Li_2O as indicated by the electron diffraction pattern (inset in Figure 1c). This finding is consistent with previous reports of "pseudo-amorphous" final phase structure, but is different from the picture that transition metal forms 1–2 nm nanocrystals in many in situ TEM studies. A detailed characterization on the final product and discussion on the electron beam effect can be found in Supporting Figure S1 and Supporting Discussion.

To reveal the reaction mechanism, Li_xWO_3 phase and W valence state evolution across the reaction front were analyzed with NBD and EELS line scan (Figure 2, Supporting Figure S2 and Supporting Movie 2). On the right side of the reaction front (e.g. position 3 and 4 in Figure 2a), diffused amorphous ring appeared in the NBDs, meaning that the structure lost crystallinity beyond the reaction front (CF). Surprisingly, near the left side of the CF, the NBD shows significant variations compared to the pristine WO_3, even though the crystallinity is well preserved.

Measurement from NBD shows that, approaching from far left to CF, the d-spacing of (002) planes slightly decreased. More obviously, at position 2 in Figure 2, some diffraction spots disappeared compared to that of pristine WO_3. Referring to known structures of Li_xWO_3,[8a] this change is consistent with gradual Li concentration increase from left to right. At position 2, the concentration reached a maximum Li intercalation value with crystalline symmetry changing from the original $P21/c$ monoclinic structure to the final intercalated cubic phase, which is also consistent with the detailed phase diagram measured by in situ X-ray diffraction (XRD) measurement.[8a,14] However, the critical maximum Li concentration that can be intercalated into WO_3 may depend critically on the dimensionality, size, and structural stability of the specific WO_3 materials. As reported by Qiang et al.,[14] the WO_3 nanorods with a high aspect ratio yield an intercalation capacity of 1.12 Li per formula unit, which is much higher than 0.5 Li per formula unit for bulk WO_3 powder as reported by Zhong et al.[8a] The maximum value of Li concentration in the final cubic phase need further evaluation using light-element-sensitive method such as atom probe tomography.[15] In addition, scanning from left to right of CF, spatial-resolved EELS spectrums (Supporting Figure S2) show that the intensity of Li K-edge gradually increased and the O_2-edge of W monotonically shifted from 56.5 eV to 54.5 eV, indicating W valence state decrease with Li^+ insertion.[2b] The structure and spectroscopy information explicitly proves that Li intercalated into the WO_3 before conversion reaction, and

the lithium concentration gradually increased in the intercalation region until conversion started at the CF. The structure evolution is illustrated by schematic models in Figure 2c. The intercalation front (IF) cannot be accurately determined (dash line in Figure 2a), because, at very low *x* values (going farther beyond the CF), Li_xWO_3 has very similar NBD pattern with pristine WO_3 and has trivial volume change and weak Li K-edge signal in the EELS spectrum. However, the distance between the CF and the point where cubic diffraction pattern is obtained (Figure 2 point 3) is ca. 60 nm, meaning that the width of intercalation region should be at least 60 nm.

With increasing Li concentration, the intercalation phase gradually transformed to amorphous starting from the CF. As shown in Supporting Figure S3a, the NBD spots of intercalation phase continuously shifted outward both tangentially and radially as shown by the red arrows. The lattice was cubic after intercalation as shown by the red square pattern of the diffraction spot. However, after further insertion of Li ions, the lattice distorted and the diffraction pattern of the original red square changed to irregular shape and finally a diffraction ring pattern appears. Ab initio molecular dynamics simulations (Supporting Figure S3b,c) consistently indicate the excessive Li ions bonded with O atoms and distorted WO_3 framework towards the formation of Li_2O and W metal ordering. A detailed analysis on the intercalation to conversion transition is provided in Supporting Information.

Similar to the case of Li^+ insertion, with continuous Na^+ insertion, the CF progressively propagated upward from the bottom contact with Na source (Figure 3a and Supporting Movie 3). Figure 3b shows a HRTEM snapshot of the CF. Fast
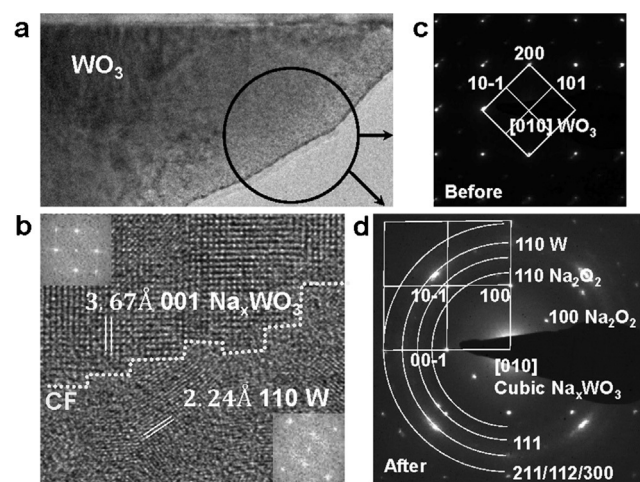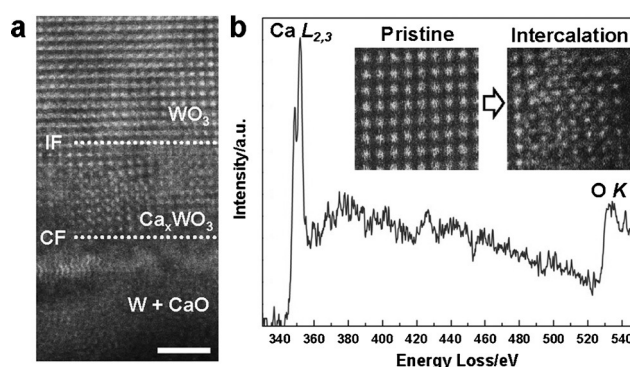

Figure 3. a) TEM image of WO_3 after Na^+ insertion. b) Atomic resolution TEM image of the conversion front. Insets show FFTs of the two sides of CF. c,d) Select area diffraction of the circled region in (a) before and after conversion.

Fourier transformations (FFT) of the local regions in the image (insets in Figure 3b) were used to analyze local phases across the CF. The FFT of the region right above the CF can only be assigned to cubic Na_xWO_3 with aligned WO_6 octahedral. The FFT of the converted region shows the formation of W nanocrystals. These phases can also be

identified from the select area diffraction (SAD) pattern in Figure 3d taken from the circled region in Figure 3a; besides the diffraction rings from the W metal and Na_2O_2, there is another set of diffraction pattern which can be assigned to the residual cubic Na_xWO_3 phase. The HRTEM and SAD provide solid evidence for the formation of cubic intercalation phase before conversion, hence support an intercalation-initiated conversion reaction.

To test whether the above mechanism holds for larger and multivalence ions, Ca^{2+} (radii 100 pm vs. Li^+ radii 76 pm)[16] insertion into WO_3 was studied using in situ TEM. Ca^{2+} insertion in WO_3 was also proved to follow the intercalation initiated conversion process. As shown by Figure 4a, electrochemical charging with Ca^{2+} transformed the structure to W

Figure 4. a) Atomic resolution HAADF-STEM image of WO_3 after Ca insertion. Scale bar, 2 nm. b) EELS spectrum of the intercalation region. Insets show enlarged atomic resolution HAADF-STEM images before and after Ca intercalation.

metal and CaO. Due to relatively large *Z* number of Ca, we were able to directly image Ca atoms in WO_3 lattice using HAADF-STEM. Figure 4b shows atomic resolution HAADF-STEM images and EELS spectrum of the intercalation region. Comparing with pristine lattice, the enhanced contrast at the centers of WO_3 unit-cells directly shows Ca atoms intercalation into the center site of the WO_3 lattice. In addition, EELS spectrum of this region showing sharp Ca L-edges further supports the intercalation. Unfortunately, the conversion only proceeded for ca. 2 nm into the film, which may be attributed to the poor diffusivity of big Ca^{2+} ions in the dense W metal layers.

In conclusion, microscopic detail of conversion reaction in WO_3 during Li^+, Na^+, and Ca^{2+} ions insertion was systematically studied. In all cases, the conversion reaction was initiated by intercalation. The intercalation reaction penetrates deeply into the lattice beyond the conversion reaction front, and gradually reduces the transition metal and increases structural symmetry and conductivity, facilitating subsequent conversion reaction. With excessive "ion-soaking", ion-oxygen bonding forms and gradually destabilizes the W framework which shrinks, distorts and finally collapses to amorphous structure. With unprecedented resolution, this work by combining experiments and ab initio MD simulations presents an atomistic full picture of conversion reaction in a conversion-type electrode material in second ion batteries.

The techniques demonstrated here can be widely applied to resolve dynamic structure and chemistry in other reaction fronts or interfaces.

[1] P. Poizot, S. Laruelle, S. Grugeon, L. Dupont, J.-M. Tarascon, *Nature* **2000**, *407*, 496–499.

[2] a) S.-W. Kim, N. Pereira, N. A. Chernova, F. Omenya, P. Gao, M. S. Whittingham, G. G. Amatucci, D. Su, F. Wang, *ACS Nano* **2015**, *9*, 10076–10084; b) M. Langell, S. Bernasek, *Phys. Rev. B* **1981**, *23*, 1584–1593; c) K. He, F. Lin, Y. Zhu, X. Yu, J. Li, R. Lin, D. Nordlund, T.-C. Weng, R. M. Richards, X.-Q. Yang, M. M. Doeff, E. A. Stach, Y. Mo, H. L. Xin, D. Su, *Nano Lett.* **2015**, *15*, 5755–5763; d) F. Wang, H. C. Yu, M. H. Chen, L. Wu, N. Pereira, K. Thornton, A. Van der Ven, Y. Zhu, G. G. Amatucci, J. Graetz, *Nat. Commun.* **2012**, *3*, 1201; e) K. He, Y. Zhou, P. Gao, L. Wang, N. Pereira, G. G. Amatucci, K.-W. Nam, X.-Q. Yang, Y. Zhu, F. Wang, D. Su, *ACS Nano* **2014**, *8*, 7251–7259.

[3] a) A. Nie, L. Y. Gan, Y. Cheng, H. Asayesh-Ardakani, Q. Q. Li, C. Z. Dong, R. Z. Tao, F. Mashayek, H. T. Wang, U. S. Schlogl, R. F. Kile, R. S. Yassar, *ACS Nano* **2013**, *7*, 6203–6211; b) L. Zhong, X. H. Liu, G. F. Wang, S. X. Mao, J. Y. Huang, *Phys. Rev. Lett.* **2011**, *106*, 248302.

[4] L. Luo, J. Wu, J. Xu, V. P. Dravid, *ACS Nano* **2014**, *8*, 11560–11566.

[5] Q. Su, D. Xie, J. Zhang, G. Du, B. Xu, *ACS Nano* **2013**, *7*, 9115–9121.

[6] K. E. Gregorczyk, Y. Liu, J. P. Sullivan, G. W. Rubloff, *ACS Nano* **2013**, *7*, 6354–6360.

[7] L. Q. Mai, B. Hu, W. Chen, Y. Y. Qi, C. S. Lao, R. S. Yang, Y. Dai, Z. L. Wang, *Adv. Mater.* **2007**, *19*, 3712–3716.

[8] a) Q. Zhong, J. Dahn, K. Colbow, *Phys. Rev. B* **1992**, *46*, 2554–2560; b) S. H. Lee, M. J. Seong, H. M. Cheong, E. Ozkan, E. C. Tracy, S. K. Deb, *Solid State Ionics* **2003**, *156*, 447–452; c) K. Qi, J. Wei, M. Sun, Q. Huang, X. Li, Z. Xu, W. Wang, X. Bai, *Angew. Chem. Int. Ed.* **2015**, *54*, 15222–15225; *Angew. Chem.* **2015**, *127*, 15437–15440.

[9] a) S. H. Lee, Y. H. Kim, R. Deshpande, P. A. Parilla, E. Whitney, D. T. Gillaspie, K. M. Jones, A. H. Mahan, S. Zhang, A. C. Dillon, *Adv. Mater.* **2008**, *20*, 3627–3632; b) W. J. Li, Z. W. Fu, *Appl. Surf. Sci.* **2010**, *256*, 2447–2452.

[10] H. Yuan, L. Jiao, J. Cao, X. Liu, M. Zhao, Y. Wang, *J. Mater. Sci. Technol.* **2004**, *20*, 41–45.

[11] Y. Du, M. Gu, T. Varga, C. Wang, M. E. Bowden, S. A. Chambers, *ACS Appl. Mater. Interfaces* **2014**, *6*, 14253–14258.

[12] J. Y. Huang, L. Zhong, C. M. Wang, J. P. Sullivan, W. Xu, L. Q. Zhang, S. X. Mao, N. S. Hudak, X. H. Liu, A. Subramanian, H. Fan, L. Qi, A. Kushima, J. Li, *Science* **2010**, *330*, 1515–1520.

[13] Y. He, D. M. Piper, M. Gu, J. J. Travis, S. M. George, S. H. Lee, A. Genc, L. Pullan, J. Liu, S. X. Mao, J. G. Zhang, C. Ban, C. Wang, *ACS Nano* **2014**, *8*, 11816–11823.

[14] W. Qiang, W. Zhenhai, J. Yeonseok, C. Jiyoung, L. Kwangyeol, L. Jinghong, *Nanotechnology* **2006**, *17*, 3116.

[15] A. Devaraj, M. Gu, R. Colby, P. Yan, C. M. Wang, J. M. Zheng, J. Xiao, A. Genc, J. G. Zhang, I. Belharouak, D. Wang, K. Amine, S. Thevuthasan, *Nat. Commun.* **2015**, *6*, 8014.

[16] A. Ponrouch, C. Frontera, F. Barde, M. R. Palacin, *Nat. Mater.* **2015**, *15*, 169–172.